This is a repository copy of *A comparative study of the effect of synthesis method on the formation of P2- and P3-Na0.67Mn0.9Mg0.1O2 cathodes*.

White Rose Research Online URL for this paper:
https://eprints.whiterose.ac.uk/201828/

Version: Published Version

PAPER • OPEN ACCESS

A comparative study of the effect of synthesis method on the formation of P2- and P3-$Na_{0.67}Mn_{0.9}Mg_{0.1}O_2$ cathodes

To cite this article: George Wilson *et al* 2023 *Mater. Res. Express* **10** 074003

View the article online for updates and enhancements.

You may also like

Materials Research Express

PAPER

A comparative study of the effect of synthesis method on the formation of P2- and P3-$Na_{0.67}Mn_{0.9}Mg_{0.1}O_2$ cathodes

George Wilson, Nik Reeves-McLaren and Rebecca Boston[*]

Materials Science and Engineering, University of Sheffield Sir Robert Hadfield Building, Mappin Street, Sheffield, S1 3JD, United Kingdom
[*]   Author to whom any correspondence should be addressed.

E-mail: r.boston@sheffield.ac.uk

Abstract

Na-ion batteries offer a way to develop large-scale energy storage necessary for the increased adoption of renewable energy sources. Layered transition metal oxide materials for electrodes can be synthesised using abundant and non-toxic materials, decreasing costs and risks compared to lithium-ion batteries. Solid state processing is commonly used for synthesis, using long calcinations at high temperatures ($>800\,°C$). Other synthetic routes, such as biotemplating, offer the opportunity to reduce reaction temperatures and times, and can enable access to different polymorphs. Here, we compare the properties of $Na_{0.67}Mn_{0.9}Mg_{0.1}O_2$ synthesised by both solid state and biotemplating, producing both P2 and P3 polymorphs to understand the differences which arise as a result of synthesis and temperature choice. We show that biotemplated P3-$Na_{0.67}Mn_{0.9}Mg_{0.1}O_2$ offers increased discharge capacity over the more commonly reported P2 phase for 50 cycles at C/5, 103 mAh g^{-1} for biotemplated P3-NMMO. Furthermore, the biotemplating samples demonstrate improved capacity after 50 cycles at C/5, and higher capacity delivered at 5C in both P2 and P3 phases over conventional solid state synthesis.

Introduction

The transition to a low carbon society requires advances in energy storage technologies. To address large-scale applications such as storage of renewable energy at point of generation, sodium-ion batteries (NIBs) are emerging as a cheap, safe, and environmentally sustainable alternative to Li-ion [1, 2]. The increased mass of sodium ions relative to lithium has meant that the specific capacities of sodium-ion batteries (NIBs) generally lag behind lithium-ion batteries, and there are still fundamental materials challenges which need to be addressed across all components of the battery [1].

Of the many candidate cathode materials for NIBs, among the most commonly reported are the layered transition metal oxides (LTMOs), which have a general formula of A_xMO_2. A_x ($0.44 \geqslant x \geqslant 1$) in this case is Na, with transition metals M, e.g., Mn or Ni [1]. Using the Delmas notation [3], LTMOs are classified according to the coordination of the Na ion by oxygen: octahedral (O) or trigonal prismatic (P) [4]; and the number of repeating metal oxide layers. O-type structures typically form at $x > 0.7$, and for P-type, $0.6 < x < 0.7$ [5, 6]. P-type stacking leads to a larger MO_2 interlayer spacing [7, 8] as a reduction in shielding from Na ions increases the electrostatic repulsion between adjacent layers [9]. This, and a more direct migration pathway [10] inherent in P-type stacking, allows for easier Na$^+$ diffusion and results in improved battery performance versus O-type stacking [4, 11–15].

The most commonly reported P-type stacking phase is P2. During cycling, this polymorph undergoes phase transitions to either O2 or OP4 at high voltages (>3.5 V) [15–18], corresponding to low Na content ($x \approx 0.3$) [19]. The O2 transition is damaging to the life of the cell, as it introduces stacking faults into the crystal structure [18]. This can be avoided by doping the host material, as seen in Mg^{2+}-doped P2-$Na_{0.67}MnO_2$ [20], P2$-Na_{0.67}Ni_{0.3}Mn_{0.7}O_2$ [21], and P2-$Na_{0.67}Mn_{0.67}Ni_{0.33}O_2$ [22]. In the latter case, 10% Mg^{2+} doping led to an increase in capacity retention after 50 cycles at 12 mA g^{-1} (C/15), from 46% in undoped materials to 95%.

Removal of Ni is also a driver for current NIB research, as a means to move away from toxic elements: Ni-free P2-$Na_{0.67}Mn_{1-y}Mg_yO_2$ ($0 \leqslant y \leqslant 0.2$) [16] is a cathode material with excellent reversibility, and capacity of 150 mAh g^{-1}, where the formation of an O2 phase upon charge is avoided explicitly due to its negative effect on cycling stability and high rate performance [22].

The other commonly reported P-type phase is P3. The capacity of most P3 materials is <130 mAh g^{-1} [23–26] and the higher-capacity P3 cathodes suffer from rapid capacity fade, particularly compared to P2 phases, often falling to below 120 mAh g^{-1} within 10 cycles [27–29]. Enhanced rate capabilities in O3 phases have been attributed to phase transitions to P3 phases [30], and so P3 remains a promising polymorph, particularly if capacity fade can be addressed. These phases are also commonly synthesised with calcination temperatures between 550°C–700°C [24, 27, 31], and show promise for application with low energy synthesis methods.

$Na_{0.67}Mn_{0.9}Mg_{0.1}O_2$ (NMMO) is an established, Ni-free cathode for use in sodium-ion batteries [13, 19, 31]. Its low molecular mass compared to Ni- and Co-containing cathodes leads to a high specific capacity. Mg-doping of the parent compound $Na_{0.67}MnO_2$ [13, 32] improves capacity retention by decreasing Jahn-Teller-induced stress on the crystal structure during redox, through reduction of the quantity of Mn^{3+}, as well as suppressing the P2↔O2 transition. A study comparing P2- and P3-NMMO [31] showed the potential of the P3 phase: a high initial capacity of 150 mAh g^{-1} at 18 mA g^{-1} (0.1 C) between 2.0–4.5 V. As with the other high capacity P3 phases, the capacity fades: 80 mAh g^{-1} after 100 cycles, and 60 mAh g^{-1} after 200 cycles. By comparison, the P2-NMMO remains steady: an initial discharge capacity of 125 mAh g^{-1}, and over 100 mAh g^{-1} after 260 cycles. The combustion synthesis used in this research [31] shows that the P3-NMMO produced contains the impurities $NaHCO_3$ and Na_2CO_3, which promote the formation of hydrated phases. These worsen the electrochemical performance through the formation of electrically insulating NaOH [33–35]. This research also uses a high voltage cut-off, favouring anionic redox which is shown to be irreversible in P3-NMMO [36].

The low synthesis temperatures required for P3 phases mean that solid state synthesis is not the most effective method as it can lead to incomplete reactions (i.e. multiple and/or electrochemically inactive phases), and particle agglomeration [28]. Low temperature synthesis methods are therefore a useful tool when targeting P3 phases. Sol-gel has been used to successfully synthesise P3 phases across a range of compositions: Chen *et al* synthesised P3-$Na_{0.66}Co_{0.5}Mn_{0.5}O_2$ [37] with capacity and capacity retention (c.100 mAh g^{-1} after 30 cycles at 170 mA g^{-1}) which exceeded that of P2-$Na_{0.66}Co_{0.5}Mn_{0.5}O_2$ (c.85 mAh g^{-1} after 30 cycles at 30 mA g^{-1}) synthesised via solid state methods [32].

Another synthesis route that has shown benefits over solid state synthesis is biotemplating [27]. Similar to sol-gel, it produces samples with small particle sizes, and is a less time-intensive process than sol-gel, and has calcination times as short as 2 h. Biotemplating is a method by which metal ions are chelated from solution by long-chain naturally occurring polymeric material [38]. The biopolymer prevents recrystallisation of the precursor materials from solution, retaining a high degree of mixing, and spatially separates ions during the early parts of calcination to prevent large-scale agglomeration. This greatly reduces the size of the materials in the reaction mixture, creating shorter diffusion pathways and leading to reduced crystallite size in the product [39]. This makes biotemplating an ideal method to access the low temperature P3 phases, as well as a lower energy way to generate cathodes overall.

P3-$Na_{0.67}Ni_{0.33}Mn_{0.67}O_2$ can be formed using dextran as the biotemplate and exhibited a capacity of 103 mAh g^{-1}, compared to 80 mAh g^{-1} in solid state synthesised P2-$Na_{0.67}Ni_{0.33}Mn_{0.67}O_2$ [27]. These capacities are low compared to other Ni-based NIBs [26], but it demonstrates that P3 cathodes can exhibit high (>100 mAh g^{-1}) specific capacities and that biotemplating is a viable route to access these. There have been few studies exploring the application of biotemplating to LTMOs beyond $Na_{0.67}Ni_{0.33}Mn_{0.67}O_2$, however.

Herein we investigate the application of biotemplating synthesis to $Na_{0.67}Mn_{0.9}Mg_{0.1}O_2$ (NMMO) cathode materials and perform a comparative study of P2- and P3-NMMO synthesised using both traditional solid state synthesis and dextran biotemplating, including the synthesis of phase-pure P3-$Na_{0.67}Mn_{0.9}Mg_{0.1}O_2$ for the first time. The aim is to understand the differences between P2 and P3 phases in the NMMO composition, and to ascertain the impact of chosen synthesis method, and use these two synthesis methods to compare the electrochemical properties of both the P2 and P3 phases.

Methodology

Synthesis

To produce solid state NMMO, dried Na_2CO_3 (Sigma Aldrich, UK, $\geqslant$ 99.5%), MnO_2 (Sigma Aldrich, UK, $\geqslant$ 99%), and MgO (Sigma Aldrich, UK, $\geqslant$ 99%) were mixed in stoichiometric amounts (with a 10% excess of Na to

counteract Na volatility during calcination) via ball milling for 8 h in isopropyl alcohol. The mixture was then dried, sieved, and manually pressed into pellets pre-calcination.

For the biotemplated samples, CH_3COONa (Sigma Aldrich, UK, $\geqslant 99\%$), $(CH_3COO)_2Mn.4H_2O$ (Alfa, $\geqslant 22\%$ Mn content by assay), $(CH_3COO)_2Mg.4H_2O$ (Sigma Aldrich, UK, $\geqslant 98\%$) were dissolved in distilled water in stoichiometric amounts (with 10% excess of Na to counteract Na volatility during calcination). Dextran (Sigma Aldrich, UK, $M_r = 70\,000$) was added to this solution in a 1:10 by weight ratio with the water. Once dissolved, the solution was dried at 80 °C to produce a hard organic-inorganic composite.

The heating protocols for both solid state and biotemplated samples were kept consistent for each phase. P3 phases were calcined at 580 °C for 20 h in air, with a 5 °C min^{-1} ramp rate, and held at 200 °C post-calcination to avoid water absorption. The P2 phases were calcined at 900 °C for 20 h in air, with a ramp of 5 °C min^{-1}, and held at 200 °C post-calcination. The resultant powders were ground in air and stored in a 120 °C vacuum oven for at least 8 h to remove any water absorbed by the structure prior to transferral into an Ar-filled glovebox.

Characterisation

All samples were analysed using x-ray diffraction (XRD) with a PANalytical X'Pert^3 Powder diffractometer with Ni-filtered Cu Kα radiation and a PIXcel^{1D} detector. Phase analysis was conducted using the ICDD PDF-4+ database and SIeve+ software. Rietveld refinements were conducted using HighScore [40], using crystal structures from Lu *et al* as starting models [41]. The background was refined first, using a 6-term shifted Chebyshev function. Sample height displacement was corrected using Si standard 640e. The lattice parameters were refined, followed by the Caglioti and peak shape profile variables. Mn and Mg occupancies were set to sum to unity, though Na occupancies were allowed to refine freely. For atomic coordinates, only the Z parameters of O and Na were refineable. Crystal structure visualisations were generated using CrystalMaker®: a crystal and molecular structures program for Mac and Windows. CrystalMaker Software Ltd., Oxford, England (www.crystalmaker.com).

Samples for scanning electron microscopy (SEM) were prepared by affixing powders to double-sided carbon tape and sputter coating with c. 15 nm thick layer of gold. Imaging was performed using an FEI Inspect F SEM. Energy-dispersive x-ray spectroscopy (EDX) was performed using an Aztec Xplore detector on an FEI Inspect F50. Average crystallite sizes were obtained via manual measurement using ImageJ [42].

Due to the volatile nature of Na, the precise stoichiometry of the material is not certain, however as the cathode materials are cycled versus Na metal, any small amount of Na lost will be replaced on the first cycle. As such any Na loss during calcination will have a negligible impact on subsequent performance. The Mn:Mg ratio in the material will affect electrochemistry, but since calcination protocols are kept consistent between phases, the Mn:Mg ratio should be consistent ($+/- 1\%$) across synthesis methods [36], allowing valid comparisons to be made between them.
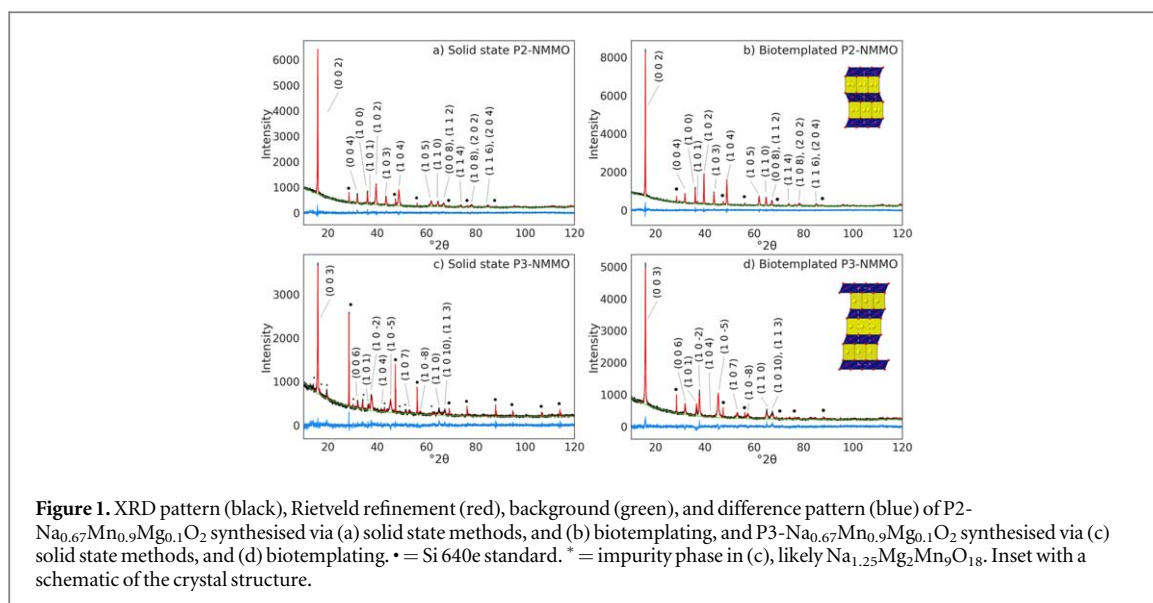
A biotemplated P3-NMMO sample, calcined at 700 °C for 2 h, was examined via inductively coupled plasma-optical emission spectroscopy (ICP-OES), conducted using a Spectro-Ciros Vision (Amatek Inc., Mahwah, NJ). The calcination temperature for the P3-NMMO samples in this study was lower, as so the ratio above is likely to be the limit with respect to compositional error. For P2-NMMO calcined at 900 °C, its composition may deviate further from that given by ICP-OES, but it is close enough in temperature that deviations are likely to be small.

Electrochemical testing

Electrodes were generated by grinding together the active material, C65 (MTI), and PVDF (MTI) in an 8:1:1 ratio. This powder was mixed in an orbital mixer with N-Methyl-2-pyrrolidone (Sigma) to form a slurry which was cast onto carbon-coated Al foil (MTI) with a 250 μm thickness. The slurry was heated in air for 1 h and cured in an 80 °C vacuum oven overnight. The electrode was calendered to approximately 50% of the original cathode thickness. 12 mm cathode discs were punched from this to use as the electrode. Electrodes had an active material loading between 3.5–5.0 mg cm^{-2}.

Cells were assembled in an Ar-filled glove box ($O_2 < 0.5$ ppm, $H_2O < 0.5$ ppm) using stainless steel 2032 coin cells (CES) containing, in order, a 0.5 mm stainless steel spacer (CES), a sodium metal counter electrode (Sigma), a glass microfibre separator (GF/6, SLS), and the working electrode. The separator was soaked in 0.085 ml of 1 M NaPF$_6$ in 1:1 EC/DEC (v/v) (Kishida).

Using a Neware Battery System, discharge capacities were determined by cycling between 1.5–4.0 V at C/5 (1C = 184 mA g^{-1}), corresponding to 0.67 mol of Na$^+$ extracted per unit of NMMO, for 50 cycles. Galvanostatic cycling was performed on at least three cells per composition, with a further cell used for rate capability testing.

Figure 1. XRD pattern (black), Rietveld refinement (red), background (green), and difference pattern (blue) of P2-$Na_{0.67}Mn_{0.9}Mg_{0.1}O_2$ synthesised via (a) solid state methods, and (b) biotemplating, and P3-$Na_{0.67}Mn_{0.9}Mg_{0.1}O_2$ synthesised via (c) solid state methods, and (d) biotemplating. • = Si 640e standard. * = impurity phase in (c), likely $Na_{1.25}Mg_2Mn_9O_{18}$. Inset with a schematic of the crystal structure.

Results and discussion

Material characterisation

XRD data shown in figures 1(a) and (b) demonstrate that both solid state and biotemplating synthesis methods produce phase pure P2-NMMO samples at 900 °C. Rietveld refinement was used to calculate the lattice parameters: P2-NMMO samples both refined to the *P6₃/mmc* space group and had lattice parameters in line with previous studies [13, 16, 19, 43]. The calculated lattice parameters for solid state and biotemplated P3-$Na_{0.67}Mn_{0.9}Mg_{0.1}O_2$ (figures 1(c) and (d)) were also in line with previous studies [11, 28, 29, 37, 44], both refining to the *R3m* space group.

The biotemplated P3-NMMO sample was found to be phase pure using the as described heating protocol, whereas the solid state P3-NMMO has several impurities: 3.4% MgO starting material, along with a 12.1% impurity identified to be $Na_{1.25}Mg_2Mn_9O_{18}$ [45]. The impurity contains Na channels, which may lead to electrochemical activity. Impurity phases are present here due to the low temperature used, however it enables a direct comparison between this and biotemplating methods. By comparison, biotemplated P3-NMMO is phase pure (figure 1(d)), highlighting the difference in product between the two methods under the same process conditions.

The calculated lattice parameters can be found in table 1. Rietveld refinements for both types of P3- and solid state P2-NMMO show Na deficiency, with all Na content values refining to $x \approx 0.43$. This is a function of the low mass and high mobility of Na^+ within the layered structure. ICP-OES of a biotemplated sample heated to 700 °C was measured to further investigate this. Assuming the Mn and Mg occupancies sum to 1, the molar ratios of the cations in the sample were 0.61 Na, 0.91 Mn, 0.09 Mg. Given the single phase nature of the biotemplated samples (and assuming that there is no amorphous material present), this indicates that the target stoichiometry has been achieved. The crystal structures of both P2- and P3-NMMO phases are confirmed to be the target space groups [46]. The lattice parameters for biotemplated P2-NMMO are in line with previous studies of this material [13, 16, 31, 47]. The solid state P2-NMMO lattice parameters are bigger than the biotemplated sample (by 0.010 Å for the *a* parameter, 0.025 Å for the *c* parameter), likely caused by minor Na^+ deficiency [19], relative to the biotemplated P2-NMMO. Both P2-$Na_{0.67}Mn_{0.9}Mg_{0.1}O_2$ samples refine well to the *P6₃/mmc* space group. The deviation of the lattice parameters from previously reported values is attributed to varying Na occupancy.

The P3-NMMO follows a similar pattern; the solid state P3-NMMO lattice parameters are larger than that of biotemplated P3-NMMO: a difference of 0.0053 Å for the *a* parameter, 0.011 Å for the *c* parameter. The obtained lattice parameters are higher than the other reported P3-NMMO values [31] which is also likely to be due to variable Na occupancy.

Solid state synthesis leads to larger lattice parameters in both polymorphs *versus* the biotemplated samples. Further investigation with e.g. inductively coupled plasma-optical emission spectroscopy (ICP-OES) is required to determine the extent of any variation in Na occupancy from the expected value. Here, however, Na occupancy will not affect the electrochemistry of the material here as the cathode is cycled against a Na metal anode, and so is not required for these inter-synthesis method comparisons.

Peak broadening was observed in both P3-NMMO samples compared to the P2-NMMO, indicating smaller single crystalline domain sizes; both P2-NMMO samples have larger crystallites due to the higher temperatures
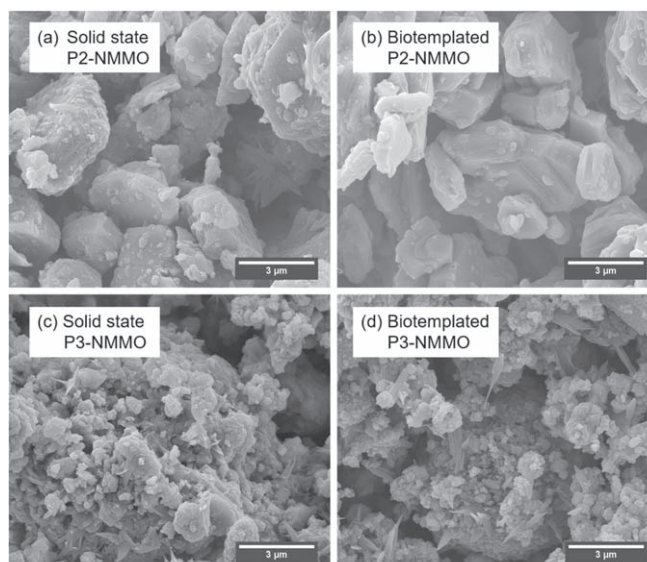
Figure 2. SEM images of (a, b) P2-$Na_{0.67}Mn_{0.9}Mg_{0.1}O_2$ synthesised via (a) solid state methods and (b) biotemplating, and P3-$Na_{0.67}Mn_{0.9}Mg_{0.1}O_2$ synthesised via (c) solid state methods and (d) biotemplating.

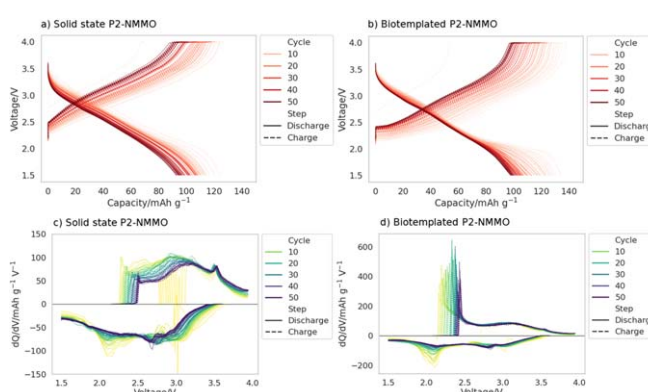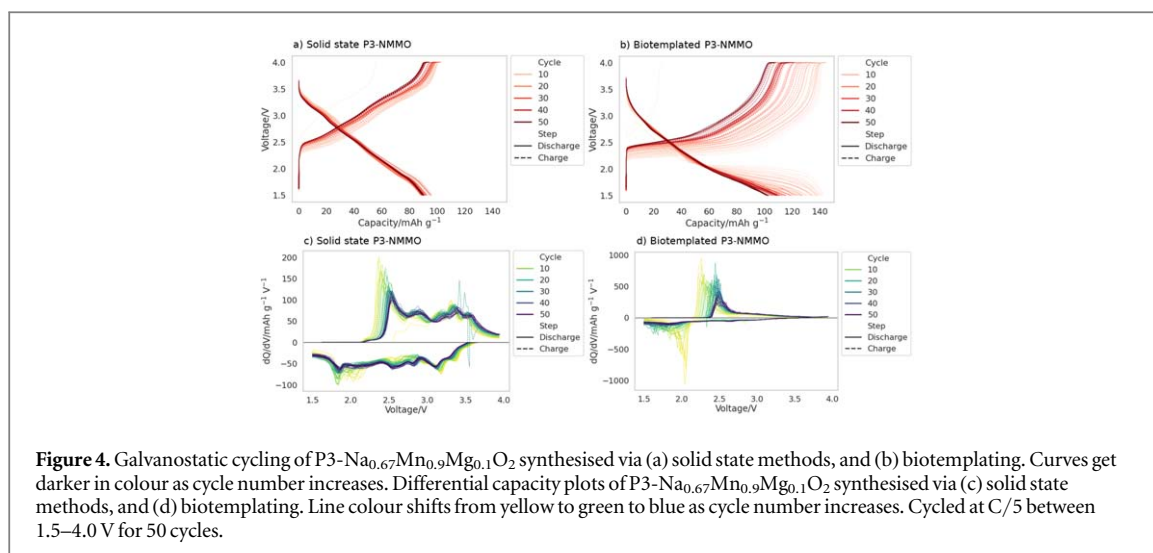**Figure 3.** Galvanostatic cycling of P2-$Na_{0.67}Mn_{0.9}Mg_{0.1}O_2$ synthesised via (a) solid state methods, and (b) biotemplating. Curves get darker in colour as cycle number increases. Differential capacity plots of P2-$Na_{0.67}Mn_{0.9}Mg_{0.1}O_2$ synthesised via (c) solid state methods, and (d) biotemplating. Line colour shifts from yellow to green to blue as cycle number increases. Cycled at C/5 between 1.5–4.0 V for 50 cycles.

Table 1. Refined structural parameters of each $Na_{0.67}Mn_{0.9}Mg_{0.1}O_2$ sample.

Sample	Space group	a (Å)	c (Å)	R_{wp} (%)	GOF
Solid state P2	$P6_3/mmc$	2.8885(5)	11.270(1)	5.558	1.0403
Biotemplated P2	$P6_3/mmc$	2.8785(1)	11.245(2)	5.501	1.0411
Solid state P3	$R3m$	2.8736(3)	16.835(1)	6.184	1.1403
Biotemplated P3	$R3m$	2.8683(3)	16.824(5)	6.130	1.1533

used. The XRD analyses are corroborated by the SEM images collected from each sample (figure 2), which illustrate a significant temperature-dependence of crystallite size between the P2- and P3-NMMO samples.

From figure 2, both P2-NMMO samples exhibit larger particle sizes than P3-NMMO and are composed of two populations of crystallites: some that are « 1.0 μm, mixed with larger (» 1.0 μm) crystallites, also observed in reports of P2-$Na_{0.67}Mn_{0.8}Mg_{0.2}O_2$ [20]. When grouped as such, the average crystallite sizes of the solid state P2-$Na_{0.67}Mn_{0.9}Mg_{0.1}O_2$ (figure 2(a)) are 0.446 μm $\pm$ 0.220 μm and 3.69 μm $\pm$ 2.04 μm, and the biotemplated P2-NMMO (figure 2(b)) 0.483 μm $\pm$ 0.195 μm and 3.39 μm $\pm$ 2.04 μm. The larger population of crystallites are in line with previous reports of P2-NMMO [13]. Both of the P3 phases were around an order of magnitude smaller in crystallite size. The solid state P3 phase (figure 2(c)) had an average of 0.36 μm $\pm$ 0.30 μm, whereas the biotemplated P3-NMMO (figure 2(d)), although well agglomerated, had an average crystallite size of

Figure 4. Galvanostatic cycling of P3-$Na_{0.67}Mn_{0.9}Mg_{0.1}O_2$ synthesised via (a) solid state methods, and (b) biotemplating. Curves get darker in colour as cycle number increases. Differential capacity plots of P3-$Na_{0.67}Mn_{0.9}Mg_{0.1}O_2$ synthesised via (c) solid state methods, and (d) biotemplating. Line colour shifts from yellow to green to blue as cycle number increases. Cycled at C/5 between 1.5–4.0 V for 50 cycles.

0.21 μm $\pm$ 0.11 μm. The size of these particles is in line with other P3 materials [27, 37], synthesised via biotemplating and sol-gel methods.

Biotemplating synthesis leads to smaller particle sizes [40] which in turn has led to improvements in electrochemical properties [23, 27, 48]. Smaller particle size gives a greater surface-area-to-volume ratio, reducing the length of diffusion pathways for Na ions. This means that per gram of material, more Na ions can be extracted or inserted at a given current, resulting in capacities closer to the theoretical value [49].

Electrochemistry

The voltage profiles of P2-NMMO, displayed in figures 3(a) and (b), show the behaviour of each sample over 50 cycles at C/5 between 1.5–4.0 V. The solid state and biotemplated P2-NMMO have discharge capacities of 110 and 118 mAh g^{-1} after the 10th cycle, falling to 94 and 98 mAh g^{-1} after 50 cycles, respectively. The initial discharge capacities for P2-NMMO are lower than those previously reported [13], but previous results use a different voltage range and electrolyte which may account for some of the differences. From cycle 20 to cycle 50 biotemplated P2-NMMO loses 10 mAh g^{-1} of capacity, whereas solid state P2-NMMO loses 15 mAh g^{-1}, showing better stability at discharge rate of C/5 when using biotemplating synthesis here.

The differential capacity plots, displayed in figures 3(c) and (d), show more clearly the voltage plateaux over cycling. Both the solid state and biotemplated P2-NMMO have similar discharge voltage profiles with respect to peak position. There are three redox pairs identified: 2.1 V/2.2 V, 2.7 V/3.0 V, and 3.1 V/3.5 V. The first two correspond to the extraction of Na$^+$ from the crystal structure. These occur at two different potentials as there are two different Na sites in the P2 structure: one edge-sharing with two MeO_2 octahedra, and one face-sharing [34], which is accompanied by Mn^{3+}/Mn^{4+} redox and Jahn-Teller distortions [19]. The first of these plateaux (2.1 V/2.2 V) in the biotemplated P2-NMMO sample continually shortens throughout cycling and is absent beyond 40 cycles. It is also present in solid state P2-NMMO but disappears more rapidly: after 30 cycles. This can be seen in the differential capacity graphs (figures 3(c) and (d)) as the reduction peak at 2.1 V is particularly strong during the first discharge cycle and by the tenth discharge cycle is much reduced. The diminution of this plateau has been observed in P2-$Na_{0.67}Mn_{0.89}Mg_{0.11}O_2$ [16], and is likely to be caused by Mn^{2+} dissolution [29, 50, 51] into the electrolyte resulting from Mn^{3+} disproportionation. The lower potential oxidation peak in the solid state P2-NMMO (figure 3(c)) both shifts to higher potentials (2.2 V to 2.4 V) and decreases slightly in intensity, although it was greatly attenuated compared to the equivalent peak in biotemplated P2-NMMO. In both, there is an oxidation peak at 3.5 V, known to be associated with the P2↔OP4 phase transition [12, 13, 18].

The results of the same cycling regime in P3-NMMO are shown in figure 4. Solid state P3-NMMO delivers initial specific capacities of 94 mAh g^{-1}, falling to 89 mAh g^{-1} after 50 cycles. Biotemplated P3-NMMO delivers a capacity of 142 mAh g^{-1} initially, decreasing to 103 mAh g^{-1} after 50 cycles (figures 4(a) and (b), respectively). Differential capacity plots of solid state and biotemplated P3-NMMO (figures 4(c) and (d), respectively) show that the two samples both exhibit a redox couple at 2.1 V/2.2 V, which is attributed to the P3↔O3 phase transition [25, 52–54], although it is greatly reduced in intensity in the solid state P3-NMMO. In the case of solid state P3-NMMO (figure 4(a)), the presence of a very short voltage plateau at 1.9 V suggests the P3↔O3 transition does occur but only to a minor extent, and so little structural degradation occurs. The capacity remains stable albeit lower than is observed in the biotemplated P3 sample. One reason for the apparent lack of P3↔O3

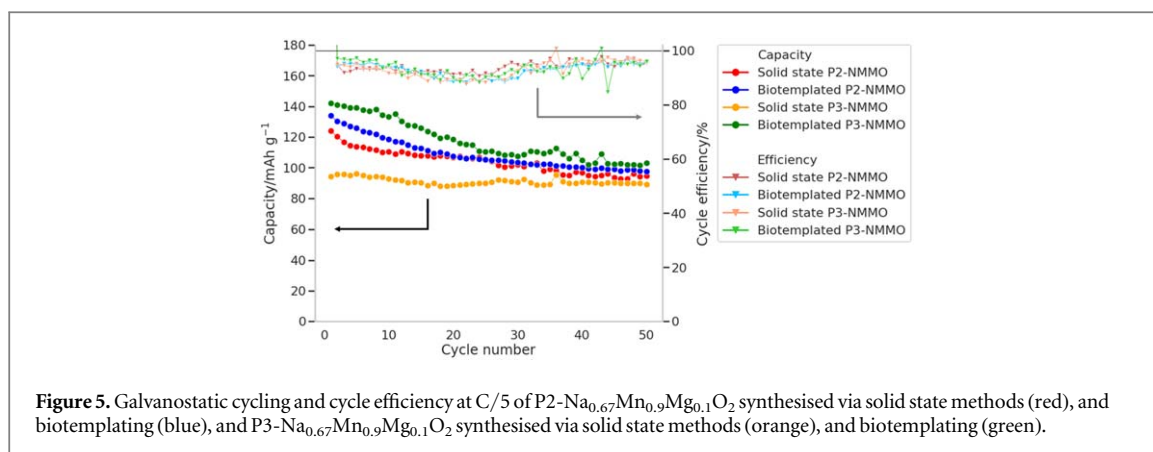**Figure 5.** Galvanostatic cycling and cycle efficiency at C/5 of P2-$Na_{0.67}Mn_{0.9}Mg_{0.1}O_2$ synthesised via solid state methods (red), and biotemplating (blue), and P3-$Na_{0.67}Mn_{0.9}Mg_{0.1}O_2$ synthesised via solid state methods (orange), and biotemplating (green).

Figure 6. Discharge capacity versus cycle number of P2-$Na_{0.67}Mn_{0.9}Mg_{0.1}O_2$ synthesised via solid state methods (red), and biotemplating (blue), and P3-$Na_{0.67}Mn_{0.9}Mg_{0.1}O_2$ synthesised via solid state methods (orange), and biotemplating (green) at different C-rates as indicated on the graph.
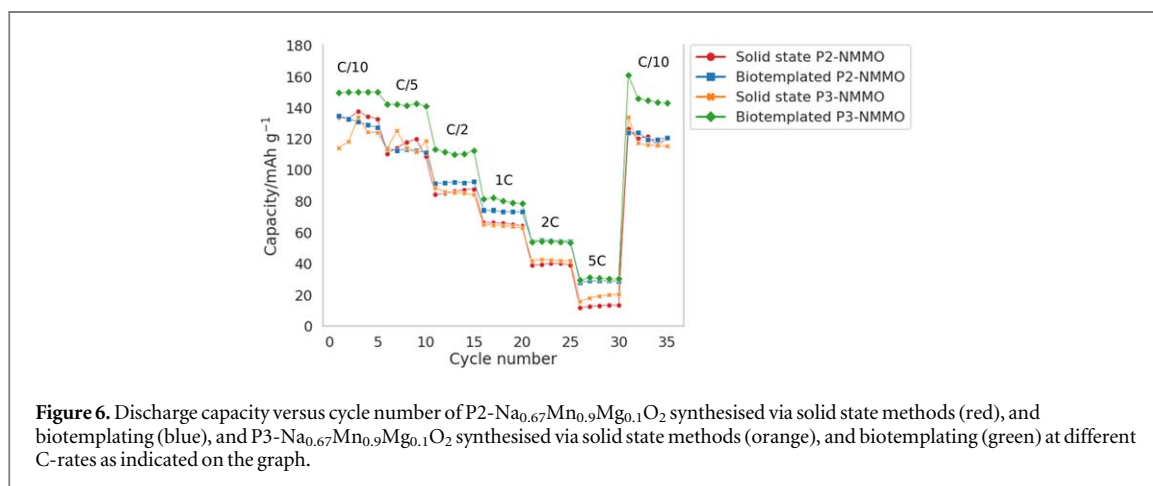
transition in solid state P3-NMMO could be the presence of an impurity phase within the cathode, akin to the use of biphasic intergrowth structures to suppress P2↔O2 [55] or P2↔OP4 [56] transitions.

Biotemplated P3-NMMO shows a long voltage plateau at 2.1 V, relating to the P3↔O3 transition. The initial measured capacities of biotemplated P3-NMMO is among the highest capacities of any previously reported P3 material [24, 25, 31], due to the low molecular mass of the cathode, and the optimised voltage range used. The plateau fades as cycling continues, accompanied by a drop in capacity over 25 cycles, at which point the plateau has devolved into a slope. This suggests a degradation within the cell or cathode structure. The result is an increase in internal resistance meaning that processes require higher overpotentials [57, 58], and a capacity that, while high, fades over time. This is shown in figure 4(d), in which the redox pair becomes more polarised at higher cycle numbers. This degradation could be attributed to dissolution of Mn^{2+} into the electrolyte, as with P2-NMMO, due to the smaller particle sizes [29], but it has not been deconvoluted from the degradation of the P3↔O3 phase transition. Since there is little capacity decay in solid state P3-NMMO the effect from manganese dissolution in biotemplated P3-NMMO is unlikely to be a major contributing factor, as the particle size of the two P3-NMMO samples is comparable.

The redox peaks in both samples, but particularly in the biotemplated P3-NMMO sample, attenuate and polarise due to degradation within the cell and the subsequent increase in internal resistance. Solid state P3-NMMO undergoes numerous additional processes absent in biotemplated P3-NMMO, as evidenced by the number of different peaks in the differential capacity graph (figures 4(c) and (d), respectively). One explanation for this may be that the impurity phases found in the solid state P3-NMMO XRD (figure 1(c)) are redox active. The crystal structure of the $Na_{1.25}Mg_2Mn_9O_{18}$ impurity contains Na^+ channels, and so a Na^+ diffusion pathway is present, as is the possibility of Na^+ (de)intercalation based on the Mn^{3+}/Mn^{4+} redox couple, as the average Mn oxidation state in the impurity phase should be +3.42. Since there are few other differences between the two P3-NMMO samples with respect to crystal structure or particle size, the impurity phase may undergo several redox processes while suppressing the P3↔O3 transition.

A comparison of the capacities and cycle efficiencies of all four samples are displayed in figure 5. The cycle efficiency of all four samples are approximately equal and follow the same trend; starting at 95% initially, it falls steadily until cycle 30. At this point, the efficiency increases and remains steady (with some fluctuations) at 95%. Most capacity degradation is seen in the first 30 cycles, leading to lower efficiencies. The likelihood of Mn2+

dissolution from the cathode into the electrolyte has been discussed, and could be the cause of low (<98%) efficiencies [59]. Both P2-NMMO samples have a lower capacity than biotemplated P3-NMMO. Previous studies into P2 and P3 materials either show a P2 phase that outperforms P3 [24] or a P3 phase that exhibits capacity decay such that it displays a lower discharge capacity than the P2 phase after 15 cycles [31]. In those studies, the upper voltage cut-off is either 4.4 V [24] or 4.5 V [31], encouraging anionic redox reaction [31], which is shown to be irreversible in the P3 material. The lower voltage cut-off is set to 2.0 V, limiting the P3↔O3 transition, where much of the P3 capacity arises. Hence the higher capacity of the biotemplated P3-NMMO relative to previous studies into P2 and P3 phases. The lower capacity of the solid state P3-NMMO is due to the lack of P3↔O3 transition, likely caused by the impurity phases identified *via* XRD, as this is the most significant difference between this sample and biotemplated P3-NMMO. This highlights the importance of selection of synthesis method to obtain cathode materials that are free of impurities that can undermine electrochemical performance.

The results from rate capability testing (figure 6) show similar patterns: higher capacity for biotemplated cells, which becomes clearer at higher C-rates. Comparing the capacities at different C-rates of each phase, a biotemplating approach to cathode manufacture favours higher capacity above C/2 for both P2 and P3 phases. The biotemplated P3-NMMO outperforms its solid state counterpart, and both P2-NMMO samples at all current densities, indicating its suitability as a high capacity cathode, even above that of the P2 phase. The better rate performance of P3-NMMO over P2 phases is expected [24]. There will be several effects here: the lower voltage cut-off of 1.5 V allows the P3↔O3 transition to occur, unlike in other comparative studies [24, 31], both of which have a lower limit of 2.0 V. Although it may increase the chance for degradation by manganese dissolution and loss of active material, the P3-NMMO sample has smaller particle sizes than either P2-NMMO sample which has been shown to improve battery performance [27, 48, 60].

The capacity of all four samples at high C-rates is lower than reported previously [19, 31] The head-to-head comparison here shows that biotemplated samples outperform those made by solid state, and that P3-NMMO has high specific capacity and higher rate capability than P2-NMMO. The higher temperatures used to form P2 phases could be resulting in sodium loss, although this is not reflected in the Rietveld refinements. The reduced performance in the solid state P3-NMMO can be attributed to the presence of secondary phases, indicating an incomplete reaction, although it further investigation of the role of this phase is needed to ascertain its effect in stabilising the P3↔O3 phase transitions.

Conclusion

In summary we have presented a comparison of chemical, physical, and electrochemical properties of NMMO synthesised by two methods. Biotemplating can be used to selectively synthesise either the P2 or P3 phase through choice of temperature, in contrast to solid state methods which can only be reliably used to produce the thermodynamic P2 product. The solid state P3-NMMO contained several impurity phases which have negatively impacted its capacity. We have demonstrated that the rarely observed P3-NMMO delivers 133 mAh g^{-1} after 10 cycles using a biotemplating synthesis, 40 mAh g^{-1} more than its solid state equivalent.

Similarly, biotemplated P3-NMMO sample delivers 20 mAh g^{-1} higher capacity than both P2-NMMO cathodes after 10 cycles, although this is lessened throughout cycling as the P3↔O3 transition diminishes. Furthermore, at high C-rates (5C), both P2 and P3 biotemplated samples deliver capacities 10–15 mAh g^{-1} higher than the solid state samples. However, at C/5 the solid state and biotemplated P2-NMMO samples deliver comparable capacities after 20 cycles.

The strengths of the biotemplating synthesis are its shorter, less labour intensive process. We have shown that it offers at least similar battery performance, and improved in several aspects, including high C-rate cycling and capacity in the P3-NMMO system. Combined with the option of vastly reduced calcination times [27] and access to phase-pure low temperature phases, the biotemplating synthesis method shows clear benefits for generating cathodes over solid state synthesis.

Acknowledgments

Data availability statement

All data that support the findings of this study are included within the article (and any supplementary files).

ORCID iDs

Rebecca Boston https://orcid.org/0000-0002-2131-2236

References

[1] Tapia-Ruiz N *et al* 2021 2021 Roadmap for sodium-ion batteries *J. Phys.: Energy* **3** 031503–92

[2] Blomgren G E 2017 The development and future of lithium ion batteries *J. Electrochem. Soc.* **164** A5019

[3] Delmas C, Fouassier C and Hagenmuller P 1980 Structural classification and properties of the layered oxides *Phys. B+C* **99** 81–5

[4] Yabuuchi N, Kubota K, Dahbi M and Komaba S 2014 Research development on sodium-ion batteries *Chem. Rev.* **114** 11636–82

[5] Han M H, Gonzalo E, Singh G and Rojo T 2015 A comprehensive review of sodium layered oxides: powerful cathodes for Na-ion batteries *Energy Environ. Sci.* **8** 81–102

[6] Slater M D, Kim D, Lee E and Johnson C S 2013 Sodium-ion batteries *Adv. Funct. Mater.* **23** 947–58

[7] Bianchini M *et al* 2018 Layered P2-O3 sodium-ion cathodes derived from Earth abundant elements *J. Mater. Chem.* A **6** 3552–9

[8] Song X *et al* 2018 Synthesis of $Na_xMn_{0.54}Ni_{0.13}Fe_{0.13}O_2$ with P2-type hexagonal phase as high-performance cathode materials for sodium-ion batteries *J. Alloys Compd.* **732** 88–94

[9] Han M H *et al* 2016 High-performance P2-phase $Na_{2/3}Mn_{0.8}Fe_{0.1}Ti_{0.1}O_2$ cathode material for ambient-temperature Sodium-Ion batteries *Chem. Mater.* **28** 106–16

[10] Kubota K, Kumakura S, Yoda Y, Kuroki K and Komaba S 2018 Electrochemistry and Solid-State Chemistry of $NaMeO_2$ (Me = 3d Transition Metals) *Adv. Energy Mater.* (Wiley-VCH Verlag) 8, 1703416

[11] Guo S *et al* 2018 Cation-mixing stabilized layered oxide cathodes for sodium-ion batteries *Sci. Bull.* **63** 376–84

[12] Yabuuchi N *et al* 2012 P2-type $Na_x[Fe_{1/2}Mn_{1/2}]O_2$ made from Earth-abundant elements for rechargeable Na batteries *Nat. Mater.* **11** 512–7

[13] Billaud J *et al* 2014 $Na_{0.67}Mn_{1-x}Mg_xO_2$ ($0 \leqslant x \leqslant 0.2$): a high capacity cathode for sodium-ion batteries *Energy Environ. Sci.* **7** 1387–91

[14] Wang Y *et al* 2013 A zero-strain layered metal oxide as the negative electrode for long-life sodium-ion batteries *Nat. Commun.* **4** 2365

[15] Lee D H, Xu J and Meng Y S 2013 An advanced cathode for Na-ion batteries with high rate and excellent structural stability *Phys. Chem. Chem. Phys.* **15** 3304

[16] Buchholz D, Vaalma C, Chagas L G and Passerini S 2015 Mg-doping for improved long-term cyclability of layered Na-ion cathode materials - The example of P2-type $Na_xMg_{0.11}Mn_{0.89}O_2$ *J. Power Sources* **282** 581–5

[17] Yoshida H *et al* 2014 P2-type $Na_{2/3}Ni_{1/3}Mn_{2/3-x}Ti_xO_2$ as a new positive electrode for higher energy Na-ion batteries *Chem. Commun.* **50** 3677–80

[18] Lu Z and Dahn J R 2001 *In Situ* x-ray diffraction study of P2-$Na_{2/3}[Ni_{1/3}Mn_{2/3}]O_2$ *J. Electrochem. Soc.* **148** A1225

[19] Clément R J *et al* 2016 Structurally stable Mg-doped P2-$Na_{2/3}Mn_{1-y}Mg_yO_2$ sodium-ion battery cathodes with high rate performance: Insights from electrochemical, NMR and diffraction studies *Energy Environ. Sci.* **9** 3240–51

[20] Li J *et al* 2019 P2—Type $Na_{0.67}Mn_{0.8}Cu_{0.1}Mg_{0.1}O_2$ as a new cathode material for sodium-ion batteries: Insights of the synergetic effects of multi-metal substitution and electrolyte optimization *J. Power Sources* **416** 184–92

[21] Singh G *et al* 2016 High voltage Mg-Doped $Na_{0.67}Ni_{0.3-x}Mg_xMn_{0.7}O_2$ (x = 0.05, 0.1) Na-Ion cathodes with enhanced stability and rate capability *Chem. Mater.* **28** 5087–94

[22] Wang P F *et al* 2016 Suppressing the P2–O2 phase transition of $Na_{0.67}Mn_{0.67}Ni_{0.33}O_2$ by magnesium substitution for improved sodium-ion batteries *Angew. Chemie - Int. Ed.,* **55** 7445–9

[23] Guo S *et al* 2016 Understanding sodium-ion diffusion in layered P2 and P3 oxides via experiments and first-principles calculations: a bridge between crystal structure and electrochemical performance *NPG Asia Mater.* **8** e266

[24] Zhou Y N *et al* 2019 A P2/P3 composite layered cathode for high-performance Na-ion full batteries *Nano Energy* **55** 143–50

[25] Risthaus T *et al* 2019 P3 $Na_{0.9}Ni_{0.5}Mn_{0.5}O_2$ cathode material for sodium ion batteries *Chem. Mater.* **31** 5376–83

[26] Maddukuri S, Valerie P and Upadhyayula V V 2017 Synthesis and electrochemical study of new P3 type layered $Na_{0.6}Ni_{0.25}Mn_{0.5}Co_{0.25}O_2$ for sodium-ion batteries *Chemistry Select* **2** 5660–6

[27] Zilinskaite S, Rennie A J R, Boston R and Reeves-McLaren N 2018 Biotemplating: a sustainable synthetic methodology for Na-ion battery materials *J. Mater. Chem.* A **6** 5346–55

[28] Kalapsazova M *et al* 2015 P3-type layered sodium-deficient nickel-manganese oxides: a flexible structural matrix for reversible sodium and lithium intercalation *Chempluschem* **80** 1642–56

[29] Chagas L G, Buchholz D, Vaalma C, Wu L and Passerini S 2014 P-type $Na_xNi_{0.22}Co_{0.11}Mn_{0.66}O_2$ materials: linking synthesis with structure and electrochemical performance *J. Mater. Chem.* A **2** 20263–70

[30] Yoshida H, Yabuuchi N and Komaba S 2013 $NaFe_{0.5}Co_{0.5}O_2$ as high energy and power positive electrode for Na-ion batteries *Electrochem. Commun.* **34** 60–3

[31] Sambandam B *et al* 2021 Validating the structural (In)stability of P3- and P2-$Na_{0.67}Mg_{0.1}Mn_{0.9}O_2$-layered cathodes for sodium-ion batteries: a time-decisive approach *ACS Appl. Mater. Interfaces* **13** 53877–91

[32] Wang X, Tamaru M, Okubo M and Yamada A 2013 Electrode properties of P2-$Na_{2/3}Mn_yCo_{1-y}O_2$ as cathode materials for sodium-ion batteries *J. Phys. Chem. C* **117** 15545–51

[33] Sathiya M, Hemalatha K, Ramesha K, Tarascon J-M and Prakash A S 2012 Synthesis, structure, and electrochemical properties of the layered sodium insertion cathode material: $NaNi_{1/3}Mn_{1/3}Co_{1/3}O_2$ *Chem. Mater.* **24** 1846–53

[34] Hwang J Y, Myung S T and Sun Y K 2017 Sodium-ion batteries: present and future *Chem. Soc. Rev.* **46** 3529–614

[35] Lee I *et al* 2021 Cationic and transition metal co-substitution strategy of O3-type $NaCrO_2$ cathode for high-energy sodium-ion batteries *Energy Storage Mater.* **41** 183–95

[36] Kim E J *et al* 2020 Vacancy-enhanced oxygen redox reversibility in P3-type magnesium-doped sodium manganese oxide $Na_{0.67}Mg_{0.2}Mn_{0.8}O_2$ *ACS Appl. Energy Mater.* **3** 10423–34

[37] Chen X *et al* 2015 Stable layered P3/P2 $Na_{0.66}Co_{0.5}Mn_{0.5}O_2$ cathode materials for sodium-ion batteries *J. Mater. Chem.* A **3** 20708–14

[38] Schnepp Z 2013 Biopolymers as a flexible resource for nanochemistry *Angew. Chemie - Int. Ed.* **52** 1096–108

[39] Boston R 2019 *Bioinspired Inorganic Materials* ed S R Hall (Royal Society of Chemistry) no. 4 ch 1 (https://doi.org/10.1039/9781788015806)

[40] Degen T, Sadki M, Bron E, König U and Nénert G 2014 The high score suite *Powder Diffr.* **29** S13–8

[41] Lu Z, Donaberger R A and Dahn J R 2000 Superlattice ordering of Mn, Ni, and Co in layered alkali transition metal oxides with P2, P3, and O3 structures *Chem. Mater.* **12** 3583–90

[42] Schindelin J, Rueden C T, Hiner M C and Eliceiri K W 2015 The imagej ecosystem: an open platform for biomedical image analysis *Mol. Reprod. Dev* **82** 518–29

[43] Wang Q C *et al* 2019 Tuning P2-structured cathode material by Na-Site Mg substitution for Na-Ion batteries *J. Am. Chem. Soc.* **141** 840–8

[44] Buchholz D, Chagas L G, Vaalma C, Wu L and Passerini S 2014 Water sensitivity of layered P2/P3-$Na_xNi_{0.22}Co_{0.11}Mn_{0.66}O_2$ cathode material *J. Mater. Chem. A* **2** 13415–21

[45] Floros N, Michel C, Hervieu M and Raveau B 2001 Calcium insertion in the $Na_4Mn_9O_{18}$ tunnel structure: $Na_{1.1}Ca_{1.8}Mn_9O_{18}$ *J. Solid State Chem.* **162** 34–41

[46] Paulsen J M and Dahn J R 1999 Studies of the layered manganese bronzes, $Na[Mn_{1-x}M_x]O_2$ with M = Co, Ni, Li, and $[Mn_{1-x}M_x]O_2$ prepared by ion-exchange *Solid State Ionics* **126** 3–24

[47] Sharma N *et al* 2015 Rate dependent performance related to crystal structure evolution of $Na_{0.67}Mn_{0.8}Mg_{0.2}O_2$ in a sodium-ion battery *Chem. Mater.* **27** 6976–86

[48] Liu X, Wang X, Iyo A, Yu H, Li D and Zhou H 2014 High stable post-spinel $NaMn_2O_4$ cathode of sodium ion battery *J. Mater. Chem. A* **2** 14822–6

[49] Su D, Wang C, Ahn H J and Wang G 2013 Single crystalline $Na_{0.7}MnO_2$ nanoplates as cathode materials for sodium-ion batteries with enhanced performance *Chem. - A Eur. J.* **19** 10884–9

[50] Ma X, Chen H and Ceder G 2011 Electrochemical properties of monoclinic $NaMnO_2$ *J. Electrochem. Soc.* **158** A1307

[51] Terada Y, Nishiwaki Y, Nakai I and Nishikawa F 2001 Study of Mn dissolution from $LiMn_2O_4$ spinel electrodes using *in situ* total reflection x-ray fluorescence analysis and fluorescence XAFS technique *J. Power Sources* **97–98** 420–2

[52] Komaba S, Yabuuchi N, Nakayama T, Ogata A, Ishikawa T and Nakai I 2012 'Study on the reversible electrode reaction of $Na_{1-x}Ni_{0.5}Mn_{0.5}O_2$ for a rechargeable sodium-ion battery *Inorg. Chem.* **51** 6211–20

[53] Yabuuchi N, Yoshida H and Komaba S 2012 Crystal structures and electrode performance of alpha-$NaFeO_2$ for rechargeable sodium batteries *Electrochemistry* **80** 716–9

[54] Ding J J, Zhou Y N, Sun Q and Fu Z W 2012 Cycle performance improvement of $NaCrO_2$ cathode by carbon coating for sodium ion batteries,' *Electrochem. Commun.* **22** 85–8

[55] Zhai J *et al* 2022 Suppressing the irreversible phase transition from P2 to O2 in sodium-layered cathode via integrating P2- and O3-type structures *Mater. Today Energy* **29** 101106

[56] Chen C *et al* 2021 P2/O3 biphasic Fe/Mn-based layered oxide cathode with ultrahigh capacity and great cyclability for sodium ion batteries *Nano Energy* **90** 106504

[57] Tang M, Carter W C and Chiang Y-M 2010 Electrodes for lithium-ion batteries: examples in lithium metal phosphate olivines *Annu. Rev. Mater. Res.* **40** 501–29

[58] Bischoff C, Fitz O, Schiller C, Gentischer H, Biro D and Henning H-M 2018 Investigating the impact of particle size on the performance and internal resistance of aqueous Zinc Ion batteries with a manganese sesquioxide cathode *Batteries* **4** 44

[59] Ma J, Bo S H, Wu L, Zhu Y, Grey C P and Khalifah P G 2015 Ordered and disordered polymorphs of $Na(Ni_{2/3}Sb_{1/3})O_2$: honeycomb-ordered cathodes for Na-ion batteries *Chem. Mater.* **27** 2387–99

[60] Liu C, Neale Z G and Cao G 2016 Understanding electrochemical potentials of cathode materials in rechargeable batteries *Mater. Today* **19** 109–23